Journal of Materials Chemistry A

Substrate controls photovoltage, photocurrent and carrier separation in nanostructured Bi2S3 films

Journal:	*Journal of Materials Chemistry A*
Manuscript ID	TA-ART-07-2023-004276.R1
Article Type:	Paper
Date Submitted by the Author:	02-Oct-2023
Complete List of Authors:	Khan, Sherdil; Universidade Federal do Rio Grande do Sul (UFRGS), Instituto de Física Daemi, Sahar; University of California Davis, Chemistry Kanwal, Maria; UC Davis Xiao, Chengcan; University of California, Department of Chemistry Osterloh, Frank ; University of California, Department of Chemistry

Substrate controls photovoltage, photocurrent and carrier separation in nanostructured Bi_2S_3 films†

Sherdil Khan, [a,b*] Sahar Daemi, [b] Maria Kanwal, [b] Chengcan Xiao, [b] and Frank E. Osterloh [b*]

[a] Laboratory of Nanomaterials for Renewable Energy and Artificial Photosynthesis (NanoREAP), Institute of Physics, UFRGS, Av Bento Goncalves 9500, 91509-900, Porto Alegre-RS, Brazil.

*sherdil.khan@ufrgs.br

[b] Department of Chemistry, University of California, One Shields Avenue, Davis, CA 95616, USA.

*fosterloh@ucdavis.edu

† Electronic supplementary information available: *Including table for photocurrent comparison, morphological, crystallographic and surface characterizations of the substrates and the prepared films and their PEC performances.*

Abstract

Bi_2S_3 is a narrow bandgap (1.2 eV) semiconductor of interest for the construction of solar cells and photoelectrodes. While many researchers have reported on the use of Bi_2S_3 as a sensitizer for photoelectrodes, the photoelectrochemical (PEC) properties of pure Bi_2S_3 films are less documented. Here, phase pure Bi_2S_3 films (Bi/S elemental ratio of 0.66) were grown on FTO, ITO, Au, Mo substrates by electrochemical deposition of bismuth, followed by sulfurization in a single-zone tube furnace. The nanostructured Bi_2S_3 films are 5±1 μm thick and crystallize in orthorhombic Stibnite type structure. They have a bandgap of ~1.24 eV based on UV-Vis diffuse reflectance and are n-type based on a negative surface photovoltage (SPV) signal. X-ray photoelectron spectroscopy (XPS) places the Fermi level at 0.95-0.91 eV above the valence band edge. According to X-ray diffraction the substrates have no influence on the crystallographic properties of the Bi_2S_3 films. However, the PEC properties of Bi_2S_3 films in 0.5 M Na_2S(aq) are sensitively controlled by Bi_2S_3/substrate interface. Under 100 mW/cm^2 simulated solar (AM 1.5) illumination and 1.23 V_{RHE} applied bias, Bi_2S_3 photoelectrodes produce anodic photocurrents of 9.3 mA cm^{-2}, 6.1, 3.6 and 1.8 mA cm^{-2} for FTO, Mo, Au and ITO substrates, respectively, and photovoltages of 0.9 - 0.25 V. For FTO, the photocurrent reported here is among the best reported for phase pure Bi_2S_3 photoanodes. The lower performance of the other substrates is due a Schottky barrier at the Bi_2S_3/substrate interface, which retards electron transfer. These findings explain why FTO

is a preferred substrate for Bi_2S_3 photoanodes and they highlight the importance of matching substrate workfunction to the Bi_2S_3 Fermi level for efficient majority carrier extraction. Lastly, the work demonstrates the use of electrochemical deposition combined with single-zone furnace-based sulfurization as a pathway to form high-quality Bi_2S_3 films for solar energy conversion.

Keywords: Fermi level matching, Phase pure sulfide semiconductor, Substrate effect, Sulfurization protocol

Introduction

Metal chalcogenide semiconductors are emerging light absorbers for solar energy conversion applications, incl. solar cells and electrodes for photoelectrochemical (PEC) fuel generation. [1,2] Among these materials, bismuth sulfide (Bi_2S_3) stands out because of its favorable bandgap of 1.2-1.3 eV, high light absorption coefficient (α) of 10^4-10^5 /cm, and high electron (1100 cm^2/V) and hole (200 cm^2/V) mobilities and potential replacement to other sulfide materials due to its low toxicity.[3,4,5,6,7] Bi_2S_3 occurs naturally as the mineral Bismuthinite.[8] It crystallizes in the Stibnite structure, which is isomorphous with black phosphorus. The structure consists of Bi_2S_3 ribbons held together by weak van der Waals forces that can be cleaved easily. [9] Because of this property, Bi_2S_3 is used in the mechanical industry as a lubricant, but it also has been proposed as a component in optical switches, sensors, supercapacitors, in thermoelectric and optoelectronic devices. [10,11,12,13,14] To date, most studies on the PEC properties of Bi_2S_3 used the compound as a sensitizer in combination with other materials such as ZnO, TiO_2, or WO_3 for sulfite or sulfide oxidation. [15,16 ,17, 18] Reports on pure Bi_2S_3 photoanodes are rare. For example, *Liang et al* reported the fabrication of Bi_2S_3 nanowires producing 0.083 mA.cm^{-2} at 1 V vs Ag/AgCl, likely due to self-oxidation in aqueous Na_2SO_4. [19] Higher photocurrents in aqueous Na_2S (0.8 mA.cm^{-2} at −0.1 V vs SCE) were seen for Bi_2S_3 films synthesized by SILAR. [20] The highest photocurrents for sulfite/sulfide oxidation (e.g 9.48 mA.cm^{-2} at 1.23V vs RHE) were obtained for Bi_2S_3 based heterostructures fabricated by electrochemical/hydrothermal deposition. [15,16] Other than these deposition methods, WO_3 and TiO_2 were grown by

oxidizing W and Ti substrates, respectively to form Bi_2S_3 based heterostructures with promising results for sulfite/sulfide oxidation (**Table S1**). However, these photocurrents still only represent a fraction of the theoretical photocurrent (38.0 mA cm^{-2}) that can be achieved with Bi_2S_3, on the basis of its 1.24 eV bandgap.[21]

It is well known that the substrate can have a marked effect on device performance in photovoltaics and photoelectrochemistry, particularly for small band gap infrared absorbing materials. For energy devices indium doped tin oxide (ITO), fluorine-doped tin oxide (FTO), Mo, Ti, and Au coated glasses etc are used as substrates. [22,23,24,25,26,27] Compared to others, Bi_2S_3 on FTO gives the best PEC performance so far (Table S1), but the reasons for this are not entirely clear. It is noteworthy to mention that up until now, both Mo and Au have not been explored as substrates for Bi_2S_3, despite the fact that they hold significant importance in energy devices. To better understand the substrate dependence of Bi_2S_3, we conducted a systematic study of the structure, optical, electronic, and photoelectrochemical properties of Bi_2S_3 films on Mo, Au, FTO, and ITO substrates.

The growth of crystalline Bi_2S_3 films can be achieved conveniently by electrochemical deposition from colloidal sulfur suspension as shown in equations 1-3. Here, thiourea serves as a sulfur precursor in acidic solution: [28,29,30]

$$2Bi^{3+} + 3S^{2-} \rightarrow Bi_2S_3 \quad (1)$$

$$S_2O_3^{2-} + 2H^+ \rightarrow S\ (colloid) + SO_2 + H_2O \quad (2)$$

$$S\ (colloid) + 2e^- \rightarrow S^{2-}\ (-0.48\ V\ SHE) \quad (3)$$

The bottleneck in this synthesis is the instability of the sulfur colloid in water, which leads to precipitation and incorporation of elemental sulfur into the Bi_2S_3 film. Therefore, an alternative route was tried, that involved electrochemical growth of Bi films followed by sulfurization, according to equations 4 and 5. [31,32,33,34]

$$Bi^{3+}_{(aq)} + 3\ e^- \rightarrow Bi_{(s)} \quad (4)$$

$$2\ Bi + 3\ S \rightarrow Bi_2S_3 \quad (5)$$

As we will show below, phase pure Bi_2S_3 films can be obtained this way, using a standard single zone tube furnace for the sulfurization step. We also show that the

photoelectrochemical performance of these films is limited by a Schottky junction at the substrate/semiconductor interface. FTO is the only substrate that forms an ohmic contact with Bi_2S_3, which can explain the superior performance on this substrate.

Experimental Section

Bi films were obtained electrochemically from aqueous electrolyte containing 25 mM $Bi(NO_3)_3.5H_2O$ (Alfa Aeser, 99+%), 25 mM sodium ethylenediaminetetraacetate dihydrate (Na_2EDTA) (Fisher Scientific, 99%) and 1M HNO_3 (Sigma Aldrich, ACS reagent, 70%) at room temperature. 100 mL of the electrolyte was prepared in a volumetric flask by adding 1.22 g of $Bi(NO_3)_3.5H_2O$ and 0.93 g of Na_2EDTA in water, followed by adding 6.33 mL of HNO_3 (70%). Working electrodes were made from Au, FTO and ITO coated glasses and Mo foil. The Au coated glass was cleaned by rinsing with distilled water whereas FTO, Mo and ITO were cleaned by sonication in acetone and water for 20 min each and were dried in an oven at 50°C. A Pt wire served as counter electrode and a calomel electrode (3.5 M KCl) connected via a 3.5 M KCl salt bridge as reference electrode. All electrodes were contacted with nickel plated crocodile clamps. Electrodeposition was carried out in chronopotentiometry mode at –1.5 mA cm^{-2} for 30 min using a Gamry potentiostat (Interface 1010) at 60 rpm stirring at room temperature.

After deposition, the films were slowly dipped in water to remove the residual electrolyte and were left to dry in air. Sulfurization of the Bi films was conducted in a single zone tube furnace as shown in Scheme S1. The Bi electrodes were placed into a quartz tube with the Bi-coated side facing up. A quartz crucible filled with 2.5 g of powdered elemental sulfur was placed 10 cm in front of the films (Scheme S1). The tube was connected to an argon gas line (Airgas, 99.99%) and purged with a constant flow of 100 mL/min. The samples were then heated to 200°C at a rate of 5°C/min, kept at this temperature for 3h, and then heated further to 350°C at the same ramping rate. After 1h dwell time, the samples were cooled down to room temperature at 5°C/min, and removed from the quartz tube. The same sulfurization protocol was used for the pure substrates.

Characterization

The morphology of the films was studied by scanning electron microscopy (SEM, FEI SCIOS) at the operating voltages of 5 kV for SEM images and 20 kV for EDS mapping. The crystal structure of the films was studied by XRD using a Bruker D8 Discover diffractometer using Cu Kα1 X-rays (1.5406 Å). UV–vis diffuse reflectance spectra were acquired from *Thermo Scientific Evolution 220* UV-Vis spectrometer equipped with an integrating sphere. X-ray photoelectron spectroscopy was conducted via Kratos Supra XPS spectrometer with Al Kα source that generates X-ray at 1487 eV. All analyses were done in the ultra-high vacuum (UHV) analytical chamber with the pressure of 10^{-7} mbar. The survey scan was conducted at constant pass energy of 160 eV with a scan step of 1 eV, and the high-resolution core-level spectra were recorded at constant pass energy of 40 with a scan step of 0.1 eV. The spectra were calibrated by the position of adventitious C1s (284.8 eV). Surface photovoltage spectroscopy (SPS) measurements were performed in air using a vibrating gold mesh Kelvin probe (3 mm diameter, Delta PHI Besocke) with 1 mm distance from the film samples. Monochromatic radiation was provided by a 150 W Xe lamp using an Oriel Cornerstone 130 monochromator (≈ 1 mW cm^{-2}), which was not compensated for the variable light intensity of the Xe lamp. Contact potential difference (CPD) signals are reported relative to the values in the dark. Effective bandgaps were obtained through the tangent method from the photovoltage signals of the full scan spectra. Photoluminescence (PL) spectra were acquired from JASCO F-6500 spectrofluorometer for the excitation wavelength range of 300-500 nm. Photoelectrochemical (PEC) measurements were performed in a custom quartz cell using Gamry (Reference 600) potentiostat in a three-electrode setup, using Bi_2S_3 films at different substrates as working electrodes, Pt wire as counter electrode and calomel electrode (3.5 M KCl) connected via a 3.5 M KCl salt bridge as the reference electrode. A N_2 degassed (30 min) 0.5 M Na_2S solution served as electrolyte (pH 13.3). The cell was calibrated using the standard reduction potential of the hexacyanoferrate (III/II) couple. Applied potentials were converted to reversible hydrogen electrode (RHE) using the Nernst equation. Linear sweep voltammetry was conducted at a scan rate of 10 mV/s. Illumination was from a 150 W Xe lamp, calibrated to 100 mW/cm^2 using a polycrystalline silicon photovoltaic cell. Electrochemical impedance spectroscopy

was conducted under illumination at a light intensity of 100 mW/cm^2 at open circuit potential for a frequency range of 100 kHz—100 mHz with an amplitude of 10 mV.

Results and discussion

Bi_2S_3 films were fabricated on ITO, Mo, FTO, and gold substrates via the two-step electrochemical / sulfurization approach shown in **Scheme S1**. Bi films were electrodeposited galvanostatically by the reduction of $Bi(NO_3)_3$ / EDTA / 1.0 M HNO_3 solution at –1.5 mA cm^{-2} for 30 min. Here, the added EDTA served as a metal chelating agent which converts solvated Bi^{3+} ions into [Bi. EDTA]$^{-1}$ complex to shift the onset of Bi^{3+} reduction potential from 0.21 V to 0.05 V vs RHE.[35,36,37,38]

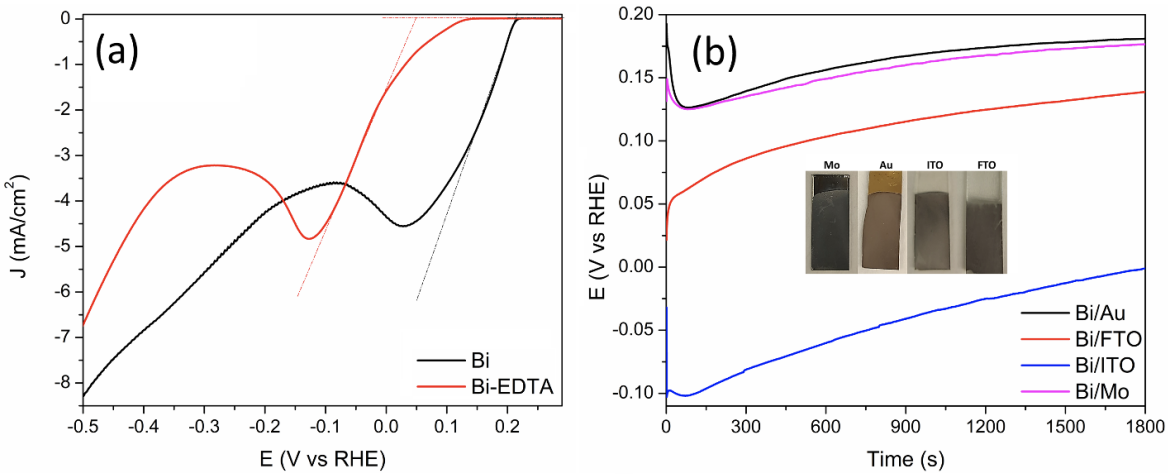

Figure 1: (a) Polarization curves for Bi deposition on FTO in 25 mM $Bi(NO_3)_3.5H_2O$ and 1M HNO_3 with and without adding 25 mM ethylenediaminetetraacetic acid disodium dihydrate (Na_2.EDTA) in the electrolyte. The dotted lines merge at the onset of Bi^{3+} reduction potential. (b) Voltage-time curves recorded during chronopotentiometry (–1.5 mA cm^{-2}) at room temperature for Au, FTO, ITO and Mo substrates. The inset shows the photographs of the as deposited films.

The applied potential variation during the galvanic deposition experiment is shown in **Figure 1b.** A sharp increase in the applied potential E_{App} during the first few seconds is related to the nucleation barrier of Bi, which requires a higher thermodynamic driving force. After approximately 150 s, E_{App} moves to more positive values. This occurs because the formed Bi crystals increase the electroactive area of the working electrode, and correspondingly, a lower overpotential is needed to keep the electrodeposition rate

constant.[39] As can be seen from **Figure 1b**, the reducing character of Bi deposition potential exhibits a distinct order: Au < Mo < FTO < ITO. Notably, this sequence aligns closely with the electrical resistance values (**Figure S1**) for these respective substrates, implying a clear correlation between the deposition potential and the ohmic resistance of the substrate which suggests the deposition potential is modulated by the substrate's ohmic resistance.

The morphologies of the as-deposited Bi films are shown in **Figure 2** (SEM images of the non-coated substrates are shown in **Figure S2**). Truncated tetrahedral crystals with irregular sizes are observed, independent of the substrate. This shows that the substrate does not affect Bi growth. [40]

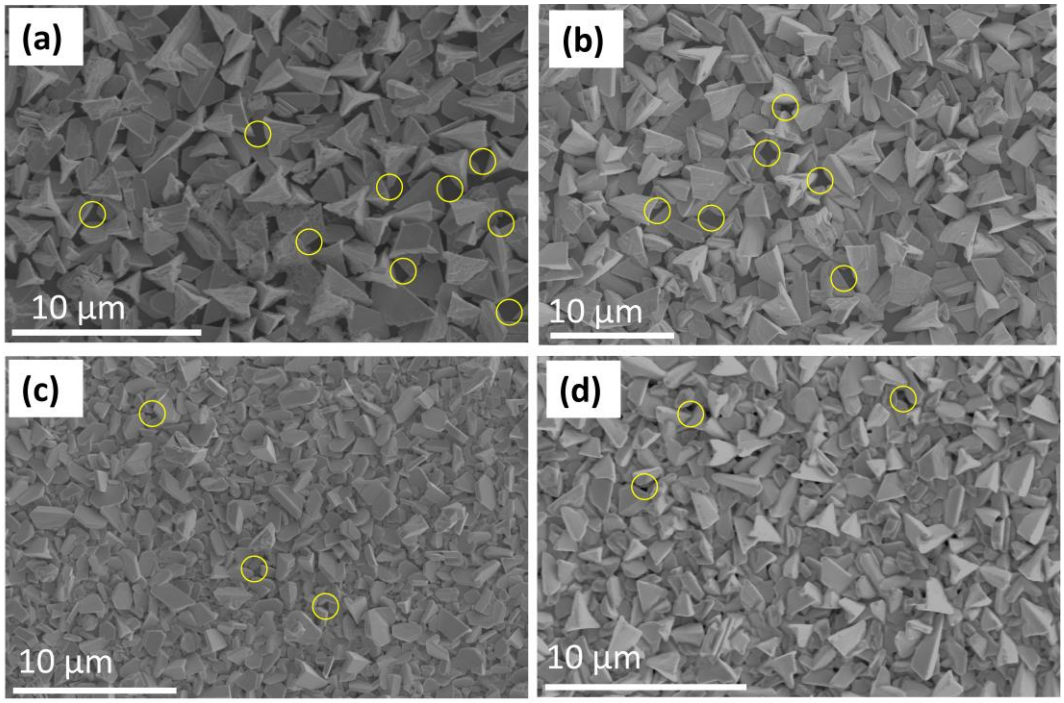

Figure 2. SEM images of as-deposited Bi films (a) FTO/Bi, (b) ITO/Bi, (c) Au/Bi and (d) Mo/Bi. The film coverage is conformal for all samples, however pinholes were observed that are highlighted as yellow circles.

Compared to the previous literature, the film coverage is more conformal,[41,42] although occasional pinholes (as can be seen in the SEM images) were observed for FTO and ITO which are attributed to substrate imperfections (**Figure S2**). As compared to FTO and ITO,

these were less apparent for Au and Mo, which might be related to the local conductivity and atomical uniformity of these substrates. Based on the appearance of pinholes, the only difference between these films was the film coverage related to the substrate irregularities, however, the morphology of the films remains the same (**Figure S2**).

In the next step, Bi films were reacted with sulfur vapor (**Scheme S1)** by two step ramping at 200°C for 3h and then at 350°C for another hour. The initial temperature was chosen above the melting point of sulfur (115.2°C) and below the melting point of Bi (271.4°C) to ensure a solid-gas phase reaction between to the elements. [43] This allows the reaction to proceed in a single temperature zone furnace, and is a major advantage over published protocols that require dual temperature zone tube furnaces. [31,32,33,34] SEM images of the resulting Bi_2S_3 films are shown in **Figure 3**. Regardless of substrate, the films are composed of irregular 1 to 6 µm particles with other smaller (~100 nm) particles on their surface (see insets). The Bi facets seen in **Figure 2** are gone and the films cover the substrates better, likely a result of the increase of the molar volume in going from Bi to Bi_2S_3.

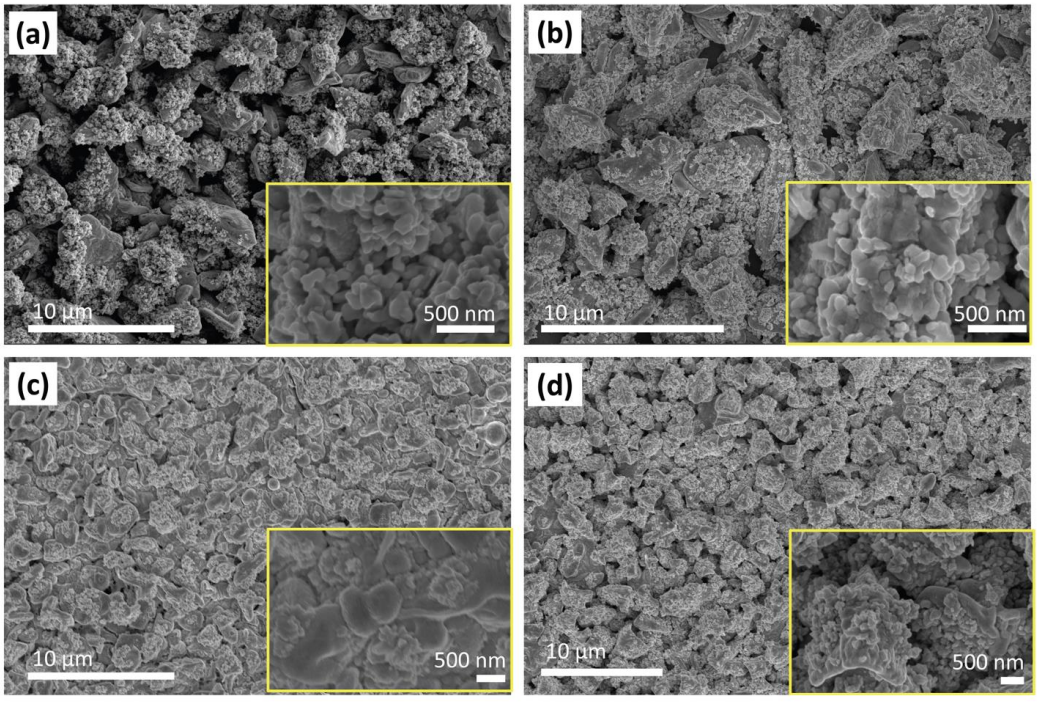

Figure 3: SEM images of (a) FTO/Bi_2S_3 (b) ITO/Bi_2S_3, (c) Au/Bi_2S_3 and (d) Mo/Bi_2S_3. The insets show the higher magnification images of the samples. After sulfurization, the surface of the films turned rougher with the appearance of some nanoparticles.

EDS mapping was employed to study the elemental chemical composition of the sulfurized film for FTO as substrate (**Figure S3**). Bi and S were found evenly distributed in the particles and the Bi/S ratio was ~0.66 corresponding to the ideal Bi_2S_3 stoichiometry. This is further supported by the EDS line scan in **Figure 4a-b**. The Bi/S relative intensity ratio does not change in the line scan which indicates the nanoparticles and the smoother microparticles are chemically identical. Based on the cross-section SEM image (**Figure 4c**) for FTO/ Bi_2S_3, the average film thickness is ~5±1 µm. EDS mapping was also employed to investigate the chemical composition of the film along the cross section (**Figure S3b**). Bi and S are uniformly distributed with an elemental ratio of ~0.63, thus showing an ideal stoichiometry along the cross-section of the film. In the current study, to ensure the reproducibility, the films were prepared galvanostatically on four different substrates at mild electrochemical conditions (–1.5 mA for 30 min (q = –2.7 C)) via chronopotentiometry (**Figure 1b**). [44] For the diffusion-controlled process, the current that passes through the electrode controls the nucleation and the formation of the films. Since all films were deposited at similar chemical and electrochemical conditions except for different substrate and the sulfurization conditions were also same for all samples which shows the nucleation and growth for Bi_2S_3 is merely heat dependant; suggesting that all prepared films should have the same thicknesses. [45] To confirm this hypothesis, the films thicknesses were determined by the SEM images of Bi_2S_3 films on other three substrates (**Figure 4d-f**). The thicknesses varied between 5 to 6 µm, showing that all deposited films possess the same thickness.

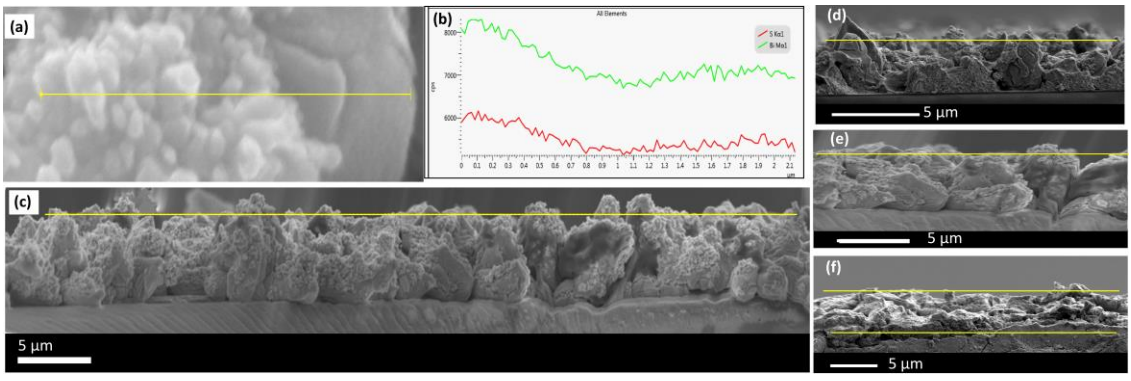

Figure 4: (a) Plain view SEM image for the EDS line scanning over smoother and rougher particles, (b) intensity vs distance graph of the line scanning showing similar relative changes for Bi and S intensities and (c) SEM cross section image for FTO/Bi_2S_3, (d) ITO/Bi_2S_3 (e) Au/Bi_2S_3 and (f) Mo/Bi_2S_3. The yellow dotted-lines are drawn for eye guide.

The surface composition of the films was studied further with X-ray photoelectron spectroscopy (XPS). The survey spectra in **Figure S4** show peaks for Bi and S and O species, likely from surface oxidation, but no other impurities. In high-resolution spectra (**Figure 5**), the Bi $4f_{7/2}$ and Bi$4f_{5/2}$ doublet was observed at the binding energies of 158.1 and 160.7 eV, respectively which correspond to the Bi^{3+} state in Bi_2S_3. From the symmetric shape of Bi4f doublet and the absence of shoulder distortion, the presence of other Bi species such as metallic Bi or Bi_2O_3 can be ruled out. However, S $2p_{3/2}$ and S $2p_{1/2}$ peaks appeared at the binding energies of 160.7 and 161.9 eV which correspond to S^{2-} valence state. [46,47] Overall, the XPS data in **Figure S4 & 5** confirms a pure Bi_2S_3 phase with no external impurities or diffusion of species from the underlying substrates.

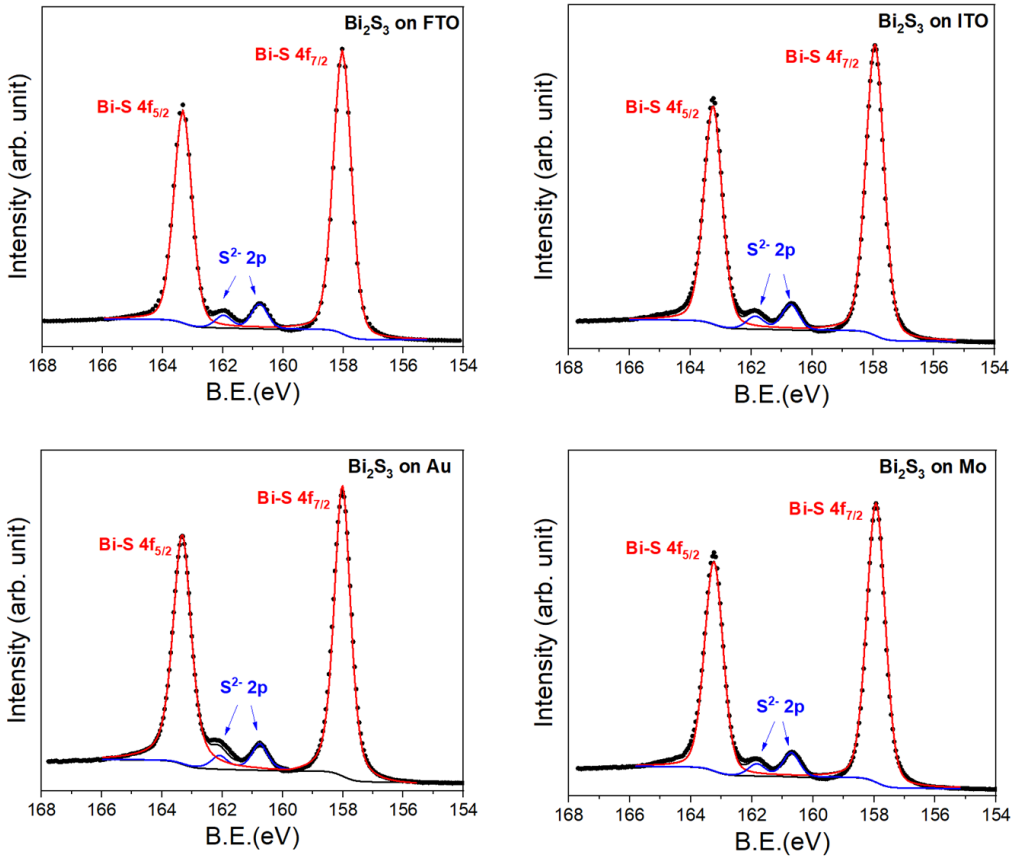

Figure 5: High resolution XPS spectra of Bi 4f and S 2p regions. The binding energy of these peaks and their symmetry correspond to Bi_2S_3 with Bi in the +3 oxidation state.

The crystal structure of the films was studied by XRD (**Figure 6**) performed in Bragg Brentano Geometry. To minimize the substrate contribution in the diffraction data, we employed an X-ray attenuator accessory during the measurements. While this approach effectively decreased the substrate influence, it should be noted that the decrease was not as pronounced for Mo and Au as observed for FTO and ITO. All diffraction peaks match well with JCPDS# 17-320 for orthorhombic Stibnite Bi_2S_3 in space group of Pbnm. The relative peak intensity ratio for the high intensity peaks ($2\theta = 25.2°$ and 28.6°) remains in the range of 0.96-0.98 for all substrates, which rules out a preferred crystal direction dependence on the substrate. [37] Furthermore, no blue/red shifts related to lattices expansion/shrinkage were observed in the peak positions suggesting that the synthesized films are crystallographically the same on each substrate. These results indicate that the bulk of the films consist of pure Bi_2S_3 phase and the substrates have no influence on the crystal growth.

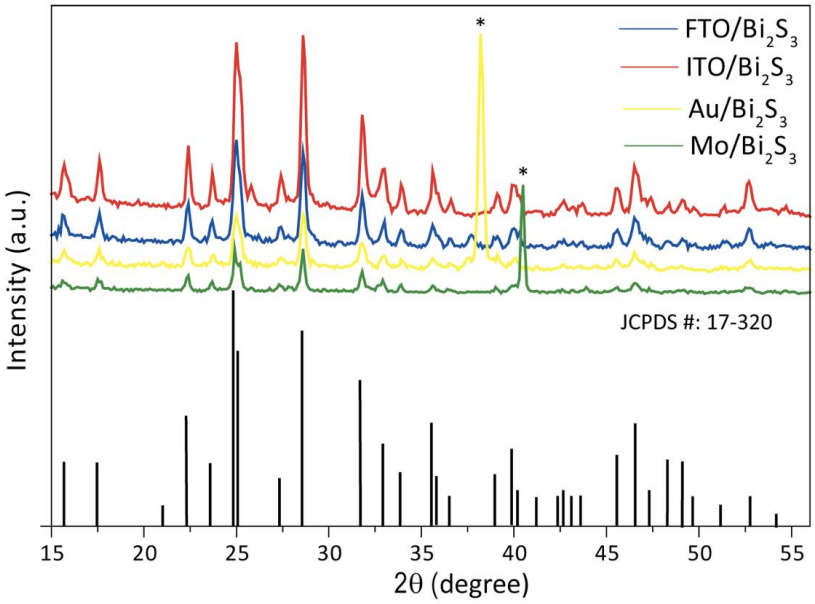

Figure 6: X-ray diffraction patterns of Bi_2S_3 films prepared on different substrates. To decrease the contributions from the substrates, a X-ray attenuator accessory was employed for data collection. Peaks marked as * for Mo/ Bi_2S_3 ($2\theta \sim 40.5°$) and Au/Bi_2S_3 ($2\theta \sim 38.3°$) correspond to the underlying Mo and Au substrates, respectively.

The optical properties of the Bi_2S_3 films were studied by UV-Vis diffuse reflectance spectroscopy (**Figure S5 & 7a**). All samples show broad light absorption below 1100 nm (>1.1 eV). A shoulder at 950-1100 nm (1.1 – 1.31 eV) is visible for films on Au and Mo substrates. Assuming that the absorption shoulder is from light reflection at the Mo and Au substrates, the band gap of Bi_2S_3 can be estimated from the tangent of the major absorption feature near 950 nm. This yields values of 1.19, 1.24, 1.26 and 1.27 eV for Au/Bi_2S_3, Mo/Bi_2S_3, ITO/Bi_2S_3 and FTO/Bi_2S_3. The average value of 1.24 eV is near the reported bandgap of Bi_2S_3 (1.2 eV) from the literature. [6]

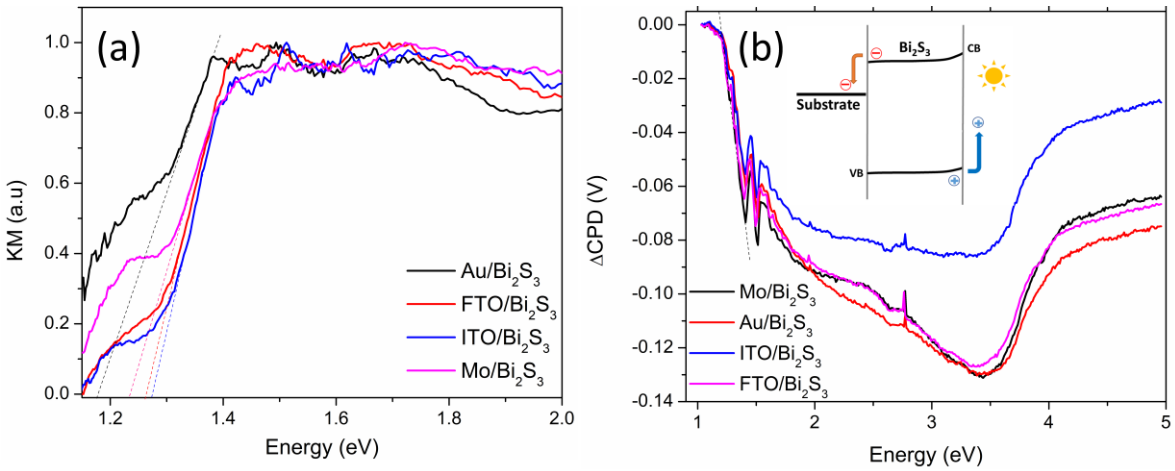

Figure 7: (a) UV-Vis diffuse reflectance spectra and (b) surface photovoltage spectra (SPS) of Bi_2S_3 on different substrates. In (b), the fine structure at 1.33 - 1.6 eV is due to strong Xe optical emission peaks at 823 nm and 882 nm and the two small features at 2.75 eV and 1.93 eV are from monochromator filter changes. The inset depicts the movement of photo-induced holes to the surface and electrons to the back contact, as for a n-type photoanode.

To determine the electronic band gap of Bi_2S_3 and the majority carrier type, surface photovoltage spectroscopy (SPS) was employed on the films. In SPS, the contact potential difference (CPD) of a sample is measured contactlessly with a vibrating gold Kelvin probe. [48] [49] [50] [51] The change of the CPD under illumination corresponds to the SPV signal, SPV = CPD(light)-CPD(dark). Spectra in **Figure 7b** show a negative SPV signal for all samples, corresponding to electron transfer away from the Kelvin probe (see insert in **Figure 7b**). This establishes electrons as majority carriers in these samples. Using a tangent to evaluate

the onset of the main SPV signal, the electronic band gap is found at 1.23 eV, similar to the optical band gap in **Figure 7a**. No mid-bandgap states were observed at lower energy. For all samples, the maximum photovoltage signal is observed at 3.5 eV, where most of the light is absorbed in the depletion layer near the Bi_2S_3 surface. At this energy, SPV=–0.13 V for all samples, except for ITO/Bi_2S_3 which shows a smaller signal (–0.086 V) [52]. This smaller signal is attributed to a larger potential drop in the more resistive ITO substrate.

Figure 8a compares linear sweep voltammetry (LSV) data under chopped light for Bi_2S_3 films immersed in aqueous Na_2S solution. Substantial anodic currents are present in the dark which reach up to 20 mA cm^{-2} (at 1.23 V vs RHE) for the Mo/Bi_2S_3 film. These currents appear above 0.50 V vs RHE and are attributed to oxidation of hydrosulfide to disulfide (0.41V vs RHE).[53] The photocurrent onsets appear slightly earlier at applied potentials of 0.2 V RHE and increase in the order ITO/Bi_2S_3 (1.8 mA cm^{-2}) < Au/Bi_2S_3 (3.6 mA cm^{-2}) < Mo/Bi_2S_3 (6.1 mA cm^{-2}) < FTO/Bi_2S_3 (9.3 mA cm^{-2}) at 1.23 V vs. RHE. This suggests the Bi_2S_3 films can generate a photovoltage of ~0.2 V in contact with the Na_2S electrolyte.

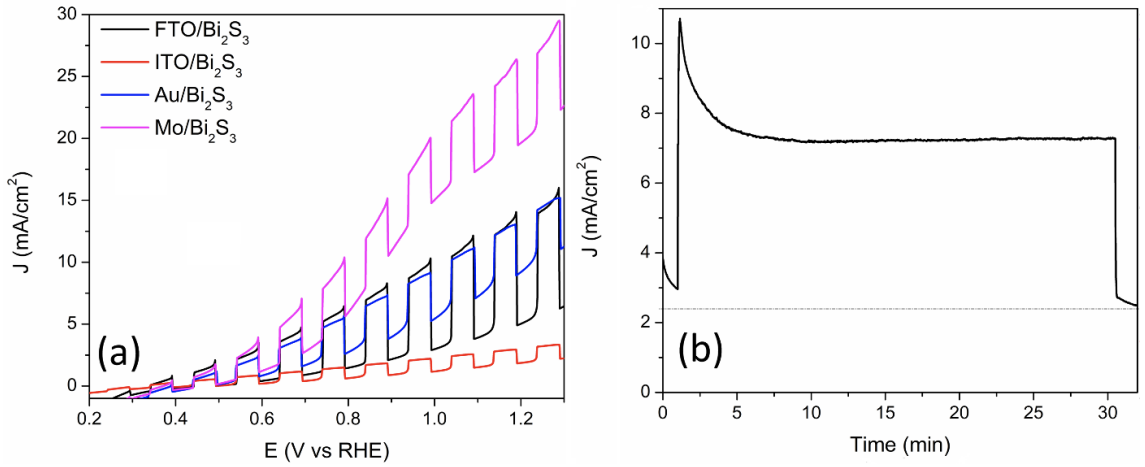

Figure 8 (a) Chopped LSV curves under chopped illumination and (b) photocurrent versus time graph for illuminated FTO/ Bi_2S_3 at 1.0 V vs RHE. All experiments were conducted in 0.5 M aqueous Na_2S (pH = 13.3) purged with N_2 gas prior to the measurements, and under illumination from Xe lamp (100 mW cm^{-2} at sample) without stirring.

To verify if the photocurrent is not merely the self-oxidation of Bi_2S_3 under illumination, a stability test was performed for the FTO/Bi_2S_3 photoelectrode. As can be seen from **Figure**

8b, illumination of the electrode under 1.0 V RHE bias produces a photocurrent spike during the first minute of the experiment, followed by a lower, but constant current, that is a result of slow HS^- transport in the non-stirred solution. The lack of any photocurrent decay over the 30 min experiment confirms that Bi_2S_3 remains stable and that the photocurrent is from HS^- oxidation.

Notably, Bi_2S_3 films prepared on FTO by sulfurization at lower temperature (200°C for 3h) or at higher temperature (350°C for 1h) produce lower photocurrents (**Figure S6a**) than the samples in **Figure 8a**. That suggests that two-step annealing process leads to a superior Bi_2S_3 with fewer defects.

To evaluate the reasons for the substantial dark current (**Figure 8a**), LSV scans were conducted for the Bi_2S_3 films without illumination (**Figure S6b**). The dark currents are similar to **Figure 8a** and have a nearly common onset of 0.50 V vs RHE, just slightly above the standard reduction potential for the HS_2^-/HS^- couple. The dark current intensity is highest for Mo/Bi_2S_3 (14.5 mA cm^{-2}) followed by Au/Bi_2S_3 (9.7 mA cm^{-2}), FTO/Bi_2S_3 (7.2 mA cm^{-2}) and ITO/Bi_2S_3 (1.9 mA cm^{-2}) at 1.23 V vs RHE. This shows that the substrates greatly influence hydrosulfide electrooxidation. To evaluate this effect, LSV scans were repeated for the bare substrates without the added Bi_2S_3 films (**Figure S7**). Interestingly, only the Mo substrate produces a significant HS^- oxidation current (58 mA cm^{-2} at 1.23 V RHE) while the currents for Au, ITO and FTO at this potential are close to zero. This data cannot explain the dark current trend in the Bi_2S_3 coated substrates seen in **Figure S8a**. However, this is not surprising considering that the substrates were likely modified during the sulfurization step in **Scheme S1**. To test the effect of sulfurization on the electrochemical behaviour of the electrodes, the bare substrates were reacted with sulfur vapor using the same two-temperature sequence as before. While the crystal structure of the sulfur-modified substrates is unchanged (**Figure S8b**) the color of the Mo and Au substrates is modified by the presence of a sulfide overlayer (**Figure S9a & 9b)**. Linear sweep voltammograms of the sulfurized substrates are shown in **Figure S7b**. The ohmic resistances of the sulfurized substrates are given in **Figure S8a**. The electrochemical currents of these substrates followed their electrical resistances trend (**Figure S8a**); thereby, the highest current density was recorded for Mo-S followed by Au-S, FTO-S and ITO-S,

respectively. Compared to their unsulfurized counterparts, the current for Mo-S was slightly decreased (45 mA cm^{-2} at 1.23 V RHE), that of Au-S was increased (15 mA cm^{-2} at 1.23 V RHE) and the currents of FTO-S and ITO-S remained unchanged. This suggests that the sulfurization of Mo and Au has a profound effect on their electrochemical behaviour. Thus, particularly for these two substrates, the sulfurized surfaces act as electrocatalysts for hydrosulfide oxidation. The electrochemical currents in **Figure S7b** now also match the dark current for the Bi_2S_3 coated films in **Figure 8a**. It is reasonable to suggest that the dark currents for the Au-Bi_2S_3 and Mo/Bi_2S_3 films in **Figure 8a** likely are from HS^- oxidation at pinholes in the films, where the Au-S and Mo-S substrates are exposed to the electrolyte. In contrast, the dark currents seen for FTO/Bi_2S_3 and ITO/Bi_2S_3 must be attributed to electrocatalytic HS^-oxidation at Bi_2S_3 sites in the film.

Next, we turn our attention to the photocurrents in **Figure 8a.** To explain the observed substrate dependence, the energy diagrams in **Scheme 1** were constructed for the FTO/Bi_2S_3 and Au/Bi_2S_3 configurations using the data in the caption. Because Bi_2S_3 is a n-type semiconductor with a reported flatband potential of 0.17 V vs RHE in sodium sulfide solution,[54] it forms a depletion layer in contact with the HS_2^-/HS^- electrolyte (0.41 V vs RHE) as shown in **Scheme 1b**. An Ohmic junction is formed with the FTO substrate, whose Fermi level (-0.04 V vs RHE) is reducing compared to that of Bi_2S_3 (0.17 V vs RHE). Illumination of the FTO/Bi_2S_3 electrode promotes hole transfer into the electrolyte and electron transfer into the substrate in agreement with the photoanodic current seen in **Figure 8a**. The situation is less optimal for the Au substrate (**Scheme 1c**), whose large workfunction causes the formation of a depletion layer in the n-Bi_2S_3 film. The resulting Schottky barrier retards electron transfer and is responsible for the lower photocurrent of the Au/Bi_2S_3 configuration, as observed in **Figure 8a**. The barrier height can be estimated as 0.89 eV, on the basis of the Fermi level difference between Au (1.06 V_{RHE}) and Bi_2S_3 (0.17 V_{RHE}). Schottky junctions with intermediate barriers form with Mo (0.39 eV) and ITO (0.17 eV), which leads to an improved photocurrent for Mo/Bi_2S_3. This Schottky-junction model explains the observed photocurrent trend in **Figure 8a**, except for ITO, whose lower performance results from the higher electric resistivity of the material (**Figure S8a**).

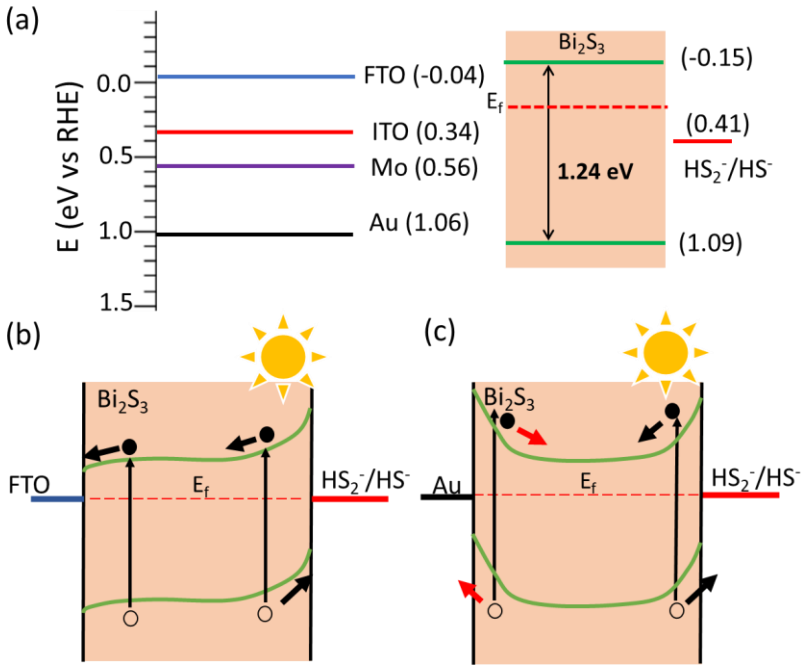

Scheme 1. (a) Workfunctions of substrates and band edges of Bi_2S_3 before contact. E_F (flat band potential) of Bi_2S_3 is ~0.17 V vs RHE in Na_2Ssolution.[54] The VB edge of Bi_2S_3 is 0.92 eV below E_F, based on valence band XPS data in **Figure S9**. This places E_{VB} at 1.09 V vs RHE in NaSH solution, and the conduction band (E_{CB}) edge at –0.15 V vs RHE, using the 1.24 eV bandgap value. Workfunctions for FTO, ITO, Mo and Au were taken from the literature as 4.4, 4.7, 5.0 and 5.5 eV, [55,56,57,58] respectively, which correspond to –0.04, 0.34, 0.56 and 1.06 V vs RHE. (b) band bending and charge transfer in FTO/Bi_2S_3/HS^- and (c) for Au/ Bi_2S_3/ SH^-. Red arrows are detrimental to photoanode performance.

The energetics in **Scheme 1** also explain the variable photovoltage of these photoelectrodes. Based the observed photocurrent onset near 0.2 V vs RHE (**Figure 8a**) and the standard reduction potential of 0.41 V vs RHE for the HS_2^-/HS^- couple, Bi_2S_3 films generate photovoltages of up to 0.25 V. To confirm this, open circuit potential measurements for the different photoanodes under AM 1.5 illumination were performed (**Figure 9a)**. Here the photovoltage is obtained as the difference between the electrochemical potentials of the photoanode under light and in the dark. The highest value (0.25 V) is seen for the FTO/Bi_2S_3 configuration, followed by ITO/Bi_2S_3 (0.19±0.01 V), Mo/Bi_2S_3 (0.12 V) and Au/Bi_2S_3 (0.09 V), respectively. This relative trend is in good agreement with the photoelectrochemical data in **Figure 8a**. It also inversely correlates with size of the detrimental Schottky barriers at the Bi_2S_3 back contact, as discussed above.

This hypothesis was also tested by Photoluminescence (PL) spectra (**Figure S11**). In agreement with the previous literature for Bi_2S_3, the main PL emission peaks were obtained at ca. ~584 nm.[59] The carrier lifetime and PL intensity are closely intertwined, as a prolonged carrier lifetime typically results in an elevated PL intensity. The reason behind this connection is that a lengthier carrier lifetime enables a greater number of carriers to undergo radiative recombination, resulting in the emission of light. In contrast, shorter carrier lifetimes tend to involve more non-radiative processes.[60] The main peak intensity decreases in order FTO>ITO>Mo>Au. This decrease followed a similar trend as observed in OCP measurements (**Figure 9a**). These analyses suggest that the work function of the substrate provides a non-radiative recombination pathway for the photogenerated carriers, thus decreasing the PL intensity according to the back contact barrier height (**Scheme 1**).

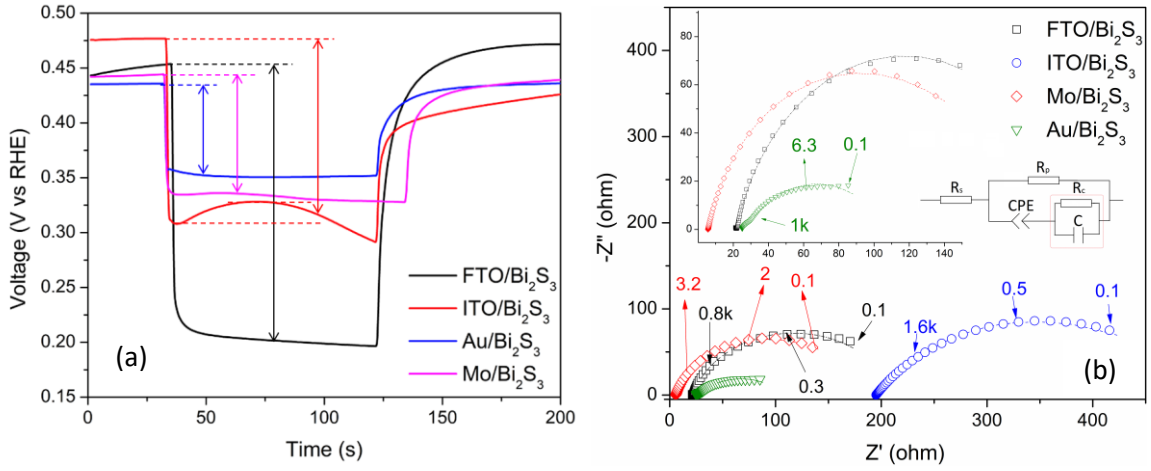

Figure 9: (a) Electrochemical potentials of Bi_2S_3 photoanodes in 0.5 M Na_2S solution measured at open circuit against saturated calomel electrode and converted to RHE. Illumination from a Xe lamp (100 mW/cm^2). (b) Nyquist plots of Bi_2S_3 films on different substrate recorded in 0.5 M Na_2S at open circuit potential under illumination. Some of the frequencies are highlighted in the data with the same colour as of the respective plots and the dotted lines show the simulated curves obtained by circuit fitting.

Electrochemical impedance spectroscopy (EIS) was utilized to study the interfacial charge transportation which was performed under 1 Sun illumination at open circuit potential in 0.5 M Na_2S. Except for Au substrate (inset **Figure 9b),** all other samples presented a single incomplete semicircle, presenting charge transfer process governed by a single time constant. [61] Data fitting was performed for an equivalent circuit which is presented in the inset of **Figure 9b** .The series resistance (R_s) simulates the solution and the back contacts

combined resistance, R_p is the resistance related to the charge transfer process at the solid-liquid junction and CPE (constant phase element) models the double layer capacitance which is added in the circuit due to the surface inhomogeneities of the electrode [62]. Particularly, for Au substrate, an additional RC component was added (highlighted in the onset of **Figure 9b**) to compensate for the second time constant process observed for this sample [54]. The fitted parameters are summarized in **Table S2**. In the current study, the observed values of the total resistance ($\sum$R) decrease in order ITO/Bi_2S_3 (510.8 **Ω**) > FTO/Bi_2S_3 (212.8 **Ω**)> Mo/Bi_2S_3 (179.8 **Ω**) > Au/Bi_2S_3 (62.6 **Ω**). It is generally expected that the photoelectrode producing better photocurrent exhibits the least overall resistance ($\sum$R). [63] For ITO/Bi_2S_3, It is reasonable to suggest the highest resistance value is related to its highest ohmic resistance (**Figure S8a**) and it also corroborates with its lowest photocurrent. However, for other substrates, the obtained resistances in EIS data values don't coincide with the observed photocurrents (**Figure 8**) trend, particularly for Au/Bi_2S_3 which is contrary to what was expected. Inline, with the literature, we observed, large dark currents in **Figure 8** for all samples.[64] As observed for FTO and ITO, pinholes do not take part in the dark current. However, the pinholes in Au/Bi_2S_3 and Mo/Bi_2S_3 act as active sites for S^{-2} oxidation in addition to the oxidation induced by Bi_2S_3 film itself. Thus, for Mo/Bi_2S_3 and Au/Bi_2S_3 smaller total resistance compared to FTO/Bi_2S_3 in the Nyquist plots can be rationalized to the presence of active S^{-2} oxidation sites in the form of pinholes which decrease the overall resistance for the charge transfer process [65]. Au WF lies closer to the VB of Bi_2S_3 (**Scheme 1**), thus, photogenerated holes in Bi_2S_3 may follow an additional path for diffusion to Au back contact.[61] That might be the reason why we observed two-time constants processes in EIS for Au/ Bi_2S_3. These results suggest that the smallest total resistance observed in the Nyquist plots for Au/ Bi_2S_3 is related to the hole transfer to the back contact and the presence of active pinholes. It is worth highlighting that FTO/Bi_2S_3 presented higher resistance in EIS compared to Mo/Bi_2S_3 and Au/Bi_2S_3 (**Figure 9b**) but the photocurrent for FTO/Bi_2S_3 was the highest (**Figure 8a**) which suggests the ohmic contact prevails for improved (photo)electron transfer. On the other hand, the WF of ITO is closer to the FTO but it presented lowest photocurrent which is related to its highest ohmic resistance. Thus, the photocurrent strongly depends on the back contact energetics and the substrate resistance. To optimize the performance of the photoelectrode, it is

essential to ensure an ohmic contact between the substrate-Bi_2S_3, as well the substrate resistance should be minimized. It is worth mentioning that the photocurrent achieved in this study with the FTO/Bi_2S_3 photoanode is among the highest reported values to date.[20] This demonstrates that the two-step electrochemical deposition / sulfurization protocol used here can produce high quality Bi_2S_3 films for photoelectrochemical energy conversion.

Conclusion

Phase-pure Bi_2S_3 films in the Stibnite structure type were prepared on FTO, ITO, Au and Mo substrates using a two-step electrochemical deposition / sulfurization protocol in a single temperature zone tube furnace. The films are n-type and have a bandgap of 1.24 eV based on surface photovoltage spectroscopy. In 0.5 M Na_2S solution, the films behave as photoanodes, producing photocurrents of up to 9.3 mA cm^{-2} at 1.23 V vs RHE and photovoltages of up to 0.25 V for the FTO/Bi_2S_3/Na_2S configuration. These values are among the best reported for phase pure Bi_2S_3 photoanodes. The lower performance on ITO substrate is due to the higher ohmic resistance of this material. In EIS analyses, the interfacial resistance value for FTO substrate was higher than Au and Mo which can be understood on the basis of a detrimental Schottky barrier at the substrate-Bi_2S_3 contacts and active pinhole for S^{2-} oxidation for these substrates. Specifically for Au/Bi_2S_3, a second time constant process was observed in the EIS; suggested as the hole transfer to the back contact due to matching Au work function with the VB of Bi_2S_3. PL spectra followed a similar trend as observed for OCP values (FTO>ITO>Mo>Au), indicating that the substrate work function play a vital role for charge transfer and recombination. Using a substrate with lower resistance and having more negative fermi level for n-type semiconductor is a straight forward path to enhance the device performance. Overall, these results provide an explanation for the predominance of FTO as preferred substrate material in the Bi_2S_3 photoanode field. They also show that the electrochemical deposition / sulfurization protocol can produce high quality Bi_2S_3 films for solar energy conversion applications.

Acknowledgments:

S. Khan acknowledges the Brazilian funding agency Coordenação de Aperfeiçoamento de Pessoal de Nível Superior (CAPES) CAPES/PRINT - Call no. 41/2017 for providing funding to visit University of California Davis for developing this project. Surface photovoltage measurements were conducted with support by the U.S. Department of Energy, Office of Science, Office of Basic Energy Sciences under Award Number DOE-SC0015329. The Kratos Supra XPS instrument was funded through the US National Science Foundation under award DMR-1828238. The authors are also thankful to Dr Yayoi Takamura and Dayne Sasaki for the XRD measurements.

References

(1) Stroyuk, O.; Raevskaya, A.; Gaponik, N. Solar Light Harvesting with Multinary Metal Chalcogenide Nanocrystals. *Chem. Soc. Rev.* **2018**, *47* (14), 5354–5422. https://doi.org/10.1039/C8CS00029H.

(2) Hadke, S.; Huang, M.; Chen, C.; Tay, Y. F.; Chen, S.; Tang, J.; Wong, L. Emerging Chalcogenide Thin Films for Solar Energy Harvesting Devices. *Chem. Rev.* **2022**, *122* (11), 10170–10265. https://doi.org/10.1021/acs.chemrev.1c00301.

(3) Wang, Y.; Liu, M.; Hao, S.; Li, Y.; Li, Q.; Liu, F.; Lai, Y.; Li, J.; Wolverton, C.; Dravid, V. P.; Jiang, L. Synergistic Defect- and Interfacial-Engineering of a Bi2S3-Based Nanoplate Network for High-Performance Photoelectrochemical Solar Water Splitting. *J. Mater. Chem. A* **2022**, *10* (14), 7830–7840. https://doi.org/10.1039/D1TA09961B.

(4) Ajiboye, T. O.; Onwudiwe, D. C. Bismuth Sulfide Based Compounds: Properties, Synthesis and Applications. *Results Chem.* **2021**, *3*, 100151. https://doi.org/10.1016/j.rechem.2021.100151.

(5) Vattikuti, S. V. P.; Police, A. K. R.; Shim, J.; Byon, C. Sacrificial-Template-Free Synthesis of Core-Shell C@Bi2S3 Heterostructures for Efficient Supercapacitor and H2 Production Applications. *Sci. Rep.* **2018**, *8* (1), 4194. https://doi.org/10.1038/s41598-018-22622-0.

(6) Sirimanne, P. M.; Takahashi, K.; Sonoyama, N.; Sakata, T. Photocurrent Enhancement of Wide Bandgap Bi2O3 by Bi2S3 over Layers. *Sol. Energy Mater. Sol. Cells* **2002**, *73* (2), 175–187. https://doi.org/10.1016/S0927-0248(01)00123-4.

(7) Esparza, D.; Zarazúa, I.; López-Luke, T.; Carriles, R.; Torres-Castro, A.; Rosa, E. D. la. Photovoltaic Properties of Bi2S3 and CdS Quantum Dot Sensitized TiO2 Solar Cells. *Electrochimica Acta* **2015**, *180*, 486–492. https://doi.org/10.1016/j.electacta.2015.08.102.

(8) Krenev, V. A.; Drobot, N. F.; Fomichev, S. V. Bismuth: Reserves, Applications, and the World Market. *Theor. Found. Chem. Eng.* **2015**, *49* (4), 532–535. https://doi.org/10.1134/S0040579515040120.

(9) Li, C.; Zhao, J.; Hu, Q.; Liu, Z.; Yu, Z.; Yan, H. Crystal Structure and Transporting Properties of Bi2S3 under High Pressure: Experimental and Theoretical Studies. *J. Alloys Compd.* **2016**, *688*, 329–335. https://doi.org/10.1016/j.jallcom.2016.06.276.

(10) Miniach, E.; Gryglewicz, G. Solvent-Controlled Morphology of Bismuth Sulfide for Supercapacitor Applications. *J. Mater. Sci.* **2018**, *53* (24), 16511–16523. https://doi.org/10.1007/s10853-018-2785-3.

(11) Prieto, G.; Kafexhiu, F.; Tuckart, W. R.; Podgornik, B. Tribological Properties of Bismuth Sulfide (Bi2S3) Particles as Grease Additive for Aluminum Forming Operations. *Wear* **2022**, *506–507*, 204442. https://doi.org/10.1016/j.wear.2022.204442.
(12) Cui, L.; Hu, J.; Wang, M.; Diao, X.; Li, C.; Zhang, C. Mimic Peroxidase- and Bi2S3 Nanorod-Based Photoelectrochemical Biosensor for Signal-On Detection of Polynucleotide Kinase. *Anal. Chem.* **2018**, *90* (19), 11478–11485. https://doi.org/10.1021/acs.analchem.8b02673.
(13) Jin, R.; Li, G.; Zhang, Z.; Yang, L.-X.; Chen, G. Carbon Coated Flower like Bi2S3 Grown on Nickel Foam as Binder-Free Electrodes for Electrochemical Hydrogen and Li-Ion Storage Capacities. *Electrochimica Acta* **2015**, *173*, 458–464. https://doi.org/10.1016/j.electacta.2015.05.021.
(14) Xi, Y.; Hu, C.; Zhang, X.; Zhang, Y.; Wang, Z. L. Optical Switches Based on Bi2S3 Nanowires Synthesized by Molten Salt Solvent Method. *Solid State Commun.* **2009**, *149* (43), 1894–1896. https://doi.org/10.1016/j.ssc.2009.08.003.
(15) Yang, M.; Shi, Y.; Li, Y.; Li, H.; Luo, N.; Li, J.; Fan, J.; Zhou, A. Construction of 2D Bi2S3/CdS Nanosheet Arrays for Enhanced Photoelectrochemical Hydrogen Evolution. *J. Electron. Mater.* **2019**, *48* (10), 6397–6405. https://doi.org/10.1007/s11664-019-07447-5.
(16) Geng, Y.-Y.; Tao, C.-L.; Duan, S.-F.; San Martin, J.; Lin, Y.; Zhu, X.; Zhang, Q.-Q.; Kang, X.-W.; He, S.-S.; Zhao, Y.-X.; Li, X.; Niu, L.; Qin, D.-D.; Yan, Y.; Han, D.-X. V-Rich Bi2S3 Nanowire with Efficient Charge Separation and Transport for High-Performance and Robust Photoelectrochemical Application under Visible Light. *Front. Catal. Energy Fuels Catal. Synth. Prod. Yield* **2020**, *350*, 47–55. https://doi.org/10.1016/j.cattod.2019.08.008.
(17) Wang, Y.; Tian, W.; Chen, L.; Cao, F.; Guo, J.; Li, L. Three-Dimensional WO3 Nanoplate/Bi2S3 Nanorod Heterojunction as a Highly Efficient Photoanode for Improved Photoelectrochemical Water Splitting. *ACS Appl. Mater. Interfaces* **2017**, *9* (46), 40235–40243. https://doi.org/10.1021/acsami.7b11510.
(18) Ji, Y.; Lou, L.; Ding, W.; Hu, J.; Shao, M.; Wang, Q.; Zhang, Y.; Cong, Y. Construction of 3D Leaf-like Bi2O3-Bi2S3 Nanosheets on Fe2O3 Nanofilms and Its Photoelectrocatalytic Performance. *Electrochimica Acta* **2019**, *313*, 282–291. https://doi.org/10.1016/j.electacta.2019.05.020.
(19) Liang, Y.-C.; Li, T.-H. Controllable Morphology of Bi2S3 Nanostructures Formed via Hydrothermal Vulcanization of Bi2O3 Thin-Film Layer and Their Photoelectrocatalytic Performances. **2022**, *11* (1), 284–297. https://doi.org/10.1515/ntrev-2022-0016.
(20) Wang, Y.; Chen, J.; Jiang, L.; Sun, K.; Liu, F.; Lai, Y. Photoelectrochemical Properties of Bi2S3 Thin Films Deposited by Successive Ionic Layer Adsorption and Reaction (SILAR) Method. *J. Alloys Compd.* **2016**, *686*, 684–692. https://doi.org/10.1016/j.jallcom.2016.06.065.
(21) Smestad, G. P.; Krebs, F. C.; Lampert, C. M.; Granqvist, C. G.; Chopra, K. L.; Mathew, X.; Takakura, H. Reporting Solar Cell Efficiencies in Solar Energy Materials and Solar Cells. *Sol. Energy Mater. Sol. Cells* **2008**, *92* (4), 371–373. https://doi.org/10.1016/j.solmat.2008.01.003.
(22) Ismail, W.; El-Shafai, N. M.; El-Shaer, A.; Abdelfatah, M. Impact of Substrate Type on the Surface and Properties of Electrodeposited Cu2O Nanostructure Films as an Absorber Layer for Solar Cell Applications. *Mater. Sci. Semicond. Process.* **2020**, *120*, 105335. https://doi.org/10.1016/j.mssp.2020.105335.
(23) McShane, C. M.; Choi, K.-S. Junction Studies on Electrochemically Fabricated p–n Cu2O Homojunction Solar Cells for Efficiency Enhancement. *Phys. Chem. Chem. Phys.* **2012**, *14* (17), 6112–6118. https://doi.org/10.1039/C2CP40502D.
(24) Cheng, Y.; Xiao, C.; Mahmoudi, B.; Scheer, R.; Maijenburg, A. W.; Osterloh, F. E. Effect of Charge Selective Contacts on the Quasi Fermi Level Splitting of CuGa3Se5 Thin Film Photocathodes for Hydrogen Evolution and Methylviologen Reduction. *EES Catal.* **2023**. https://doi.org/10.1039/D2EY00062H.

(25) Luther, J. M.; Law, M.; Beard, M. C.; Song, Q.; Reese, M. O.; Ellingson, R. J.; Nozik, A. J. Schottky Solar Cells Based on Colloidal Nanocrystal Films. *Nano Lett.* **2008**, *8* (10), 3488–3492. https://doi.org/10.1021/nl802476m.

(26) Pattantyus-Abraham, A. G.; Kramer, I. J.; Barkhouse, A. R.; Wang, X.; Konstantatos, G.; Debnath, R.; Levina, L.; Raabe, I.; Nazeeruddin, M. K.; Grätzel, M.; Sargent, E. H. Depleted-Heterojunction Colloidal Quantum Dot Solar Cells. *ACS Nano* **2010**, *4* (6), 3374–3380. https://doi.org/10.1021/nn100335g.

(27) Nisika; Kaur, K.; Kumar, M. Progress and Prospects of CZTSSe/CdS Interface Engineering to Combat High Open-Circuit Voltage Deficit of Kesterite Photovoltaics: A Critical Review. *J. Mater. Chem. A* **2020**, *8* (41), 21547–21584. https://doi.org/10.1039/D0TA06450E.

(28) Saitou, M.; Yamaguchi, R.; Oshikawa, W. Novel Process for Electrodeposition of Bi2S3 Thin Films. *Mater. Chem. Phys.* **2002**, *73* (2), 306–309. https://doi.org/10.1016/S0254-0584(01)00394-7.

(29) Monteiro, T. O.; dos Santos, C. C.; do Prado, T. M.; Damos, F. S.; Luz, R. de C. S.; Fatibello-Filho, O. Highly Sensitive Photoelectrochemical Immunosensor Based on Anatase/Rutile TiO2 and Bi2S3 for the Zero-Biased Detection of PSA. *J. Solid State Electrochem.* **2020**, *24* (8), 1801–1809. https://doi.org/10.1007/s10008-020-04637-8.

(30) Georges, C.; Tena-Zaera, R.; Bastide, S.; Rouchaud, J. C.; Larramona, G.; Lévy-Clément, C. Electrochemical Deposition of Bi2S3 Thin Films Using Dimethylsulfoxide as a Solvent. *J. Electrochem. Soc.* **2007**, *154* (12), D669. https://doi.org/10.1149/1.2792244.

(31) Fernandes, P. A.; Salomé, P. M. P.; da Cunha, A. F. Precursors' Order Effect on the Properties of Sulfurized Cu2ZnSnS4 Thin Films. *Semicond. Sci. Technol.* **2009**, *24* (10), 105013. https://doi.org/10.1088/0268-1242/24/10/105013.

(32) Chow, P. K.; Singh, E.; Viana, B. C.; Gao, J.; Luo, J.; Li, J.; Lin, Z.; Elías, A. L.; Shi, Y.; Wang, Z.; Terrones, M.; Koratkar, N. Wetting of Mono and Few-Layered WS2 and MoS2 Films Supported on Si/SiO2 Substrates. *ACS Nano* **2015**, *9* (3), 3023–3031. https://doi.org/10.1021/nn5072073.

(33) Shahzad, R.; Kim, T.; Kang, S.-W. Effects of Temperature and Pressure on Sulfurization of Molybdenum Nano-Sheets for MoS2 Synthesis. *20th Int. Vac. Congr.* **2017**, *641*, 79–86. https://doi.org/10.1016/j.tsf.2016.12.041.

(34) Liu, H. F.; Antwi, K. K. A.; Wang, Y. D.; Ong, L. T.; Chua, S. J.; Chi, D. Z. Atomic Layer Deposition of Crystalline Bi2O3 Thin Films and Their Conversion into Bi2S3 by Thermal Vapor Sulfurization. *RSC Adv.* **2014**, *4* (102), 58724–58731. https://doi.org/10.1039/C4RA09896J.

(35) Sandnes, E.; Williams, M. E.; Bertocci, U.; Vaudin, M. D.; Stafford, G. R. Electrodeposition of Bismuth from Nitric Acid Electrolyte. *Electrochimica Acta* **2007**, *52* (21), 6221–6228. https://doi.org/10.1016/j.electacta.2007.04.002.

(36) Singh, A.; Kumar, D.; Thakur, A.; Gupta, N.; Shinde, V.; Saini, B. S.; Kaur, R. Galvanostatic Deposition of Manganese Oxide Films for Super Capacitive Application and Their Fractal Analysis. *Ionics* **2021**, *27* (5), 2193–2202. https://doi.org/10.1007/s11581-021-03966-6.

(37) Amano, F.; Uchiyama, A.; Furusho, Y.; Shintani, A. Effect of Conductive Substrate on the Photoelectrochemical Properties of Cu2O Film Electrodes for Methyl Viologen Reduction. *J. Photochem. Photobiol. Chem.* **2020**, *389*, 112254. https://doi.org/10.1016/j.jphotochem.2019.112254.

(38) Jiang, Y.; Liu, C.; Huang, A. EDTA-Functionalized Covalent Organic Framework for the Removal of Heavy-Metal Ions. *ACS Appl. Mater. Interfaces* **2019**, *11* (35), 32186–32191. https://doi.org/10.1021/acsami.9b11850.

(39) Yuan, Y.; Luo, G.; Li, N. New in Situ Description of Electrodepositing Multiple Nucleation Processes under Galvanostatic Stimuli. *RSC Adv.* **2021**, *11* (50), 31526–31532. https://doi.org/10.1039/D1RA04988G.

(40) Białostocka, A. M.; Klekotka, U.; Kalska-Szostko, B. The Effect of a Substrate Material on Composition Gradients of Fe-Ni Films Obtained by Electrodeposition. *Sci. Rep.* **2020**, *10* (1), 1029. https://doi.org/10.1038/s41598-019-57363-1.
(41) Yang, M.; Hu, Z. Electrodeposition of Bismuth onto Glassy Carbon Electrodes from Nitrate Solutions. *J. Electroanal. Chem.* **2005**, *583* (1), 46–55. https://doi.org/10.1016/j.jelechem.2005.04.019.
(42) Bilican, D.; Fornell, J.; Sort, J.; Pellicer, E. Electrochemical Synthesis of Bismuth Particles: Tuning Particle Shape through Substrate Type within a Narrow Potential Window. *Materials* **2017**, *10* (1). https://doi.org/10.3390/ma10010043.
(43) Lin, J.-C.; Sharma, R. C.; Chang, Y. A. The Bi-S (Bismuth-Sulfur) System. *J. Phase Equilibria* **1996**, *17* (2), 132–139. https://doi.org/10.1007/BF02665790.
(44) Kinetics and Mechanism of Electrodeposition. In *Fundamentals of Electrochemical Deposition*; 2006; pp 77–112. https://doi.org/10.1002/0470009403.ch6.
(45) Allwright, E.; Berg, D. M.; Djemour, R.; Steichen, M.; Dale, P. J.; Robertson, N. Electrochemical Deposition as a Unique Solution Processing Method for Insoluble Organic Optoelectronic Materials. *J. Mater. Chem. C* **2014**, *2* (35), 7232–7238. https://doi.org/10.1039/C4TC01134A.
(46) Wang, K.; Zhuang, J.; Chen, L.; Xu, D.; Zhang, X.; Chen, Z.; Wei, Y.; Zhang, Y. One-Pot Synthesis of AIE Based Bismuth Sulfide Nanotheranostics for Fluorescence Imaging and Photothermal Therapy. *Colloids Surf. B Biointerfaces* **2017**, *160*, 297–304. https://doi.org/10.1016/j.colsurfb.2017.09.043.
(47) Miniach, E.; Gryglewicz, G. Solvent-Controlled Morphology of Bismuth Sulfide for Supercapacitor Applications. *J. Mater. Sci.* **2018**, *53* (24), 16511–16523. https://doi.org/10.1007/s10853-018-2785-3.
(48) Gatos, H. C.; Lagowski, J. Surface Photovoltage Spectroscopy—A New Approach to the Study of High-Gap Semiconductor Surfaces. *J. Vac. Sci. Technol.* **1973**, *10* (1), 130–135. https://doi.org/10.1116/1.1317922.
(49) Zhao, J.; Osterloh, F. E. Photochemical Charge Separation in Nanocrystal Photocatalyst Films: Insights from Surface Photovoltage Spectroscopy. *J. Phys. Chem. Lett.* **2014**, *5* (5), 782–786. https://doi.org/10.1021/jz500136h.
(50) Kronik, L.; Shapira, Y. Surface Photovoltage Spectroscopy of Semiconductor Structures: At the Crossroads of Physics, Chemistry and Electrical Engineering. *Surf. Interface Anal.* **2001**, *31* (10), 954–965. https://doi.org/10.1002/sia.1132.
(51) Dittrich, T.; Fengler, S. *Surface Photovoltage Analysis of Photoactive Materials*; WORLD SCIENTIFIC (EUROPE), 2019. https://doi.org/10.1142/q0227.
(52) Kronik, L.; Shapira, Y. Surface Photovoltage Phenomena: Theory, Experiment, and Applications. *Surf. Sci. Rep.* **1999**, *37* (1), 1–206. https://doi.org/10.1016/S0167-5729(99)00002-3.
(53) Chen, M.; Dong, H.; Xue, M.; Yang, C.; Wang, P.; Yang, Y.; Zhu, H.; Wu, C.; Yao, Y.; Luo, W.; Zou, Z. Faradaic Junction and Isoenergetic Charge Transfer Mechanism on Semiconductor/Semiconductor Interfaces. *Nat. Commun.* **2021**, *12* (1), 6363. https://doi.org/10.1038/s41467-021-26661-6.
(54) Grubač, Z.; Katić, J.; Metikoš-Huković, M. Energy-Band Structure as Basis for Semiconductor n-Bi2S3/n-Bi2O3 Photocatalyst Design. *J. Electrochem. Soc.* **2019**, *166* (10), H433. https://doi.org/10.1149/2.0481910jes.
(55) Andersson, A.; Johansson, N.; Bröms, P.; Yu, N.; Lupo, D.; Salaneck, W. R. Fluorine Tin Oxide as an Alternative to Indium Tin Oxide in Polymer LEDs. *Adv. Mater.* **1998**, *10* (11), 859–863. https://doi.org/10.1002/(SICI)1521-4095(199808)10:11<859::AID-ADMA859>3.0.CO;2-1.
(56) Zhou, Y.; Shim, J. W.; Fuentes-Hernandez, C.; Sharma, A.; Knauer, K. A.; Giordano, A. J.; Marder, S. R.; Kippelen, B. Direct Correlation between Work Function of Indium-Tin-Oxide

Electrodes and Solar Cell Performance Influenced by Ultraviolet Irradiation and Air Exposure. *Phys. Chem. Chem. Phys.* **2012**, *14* (34), 12014–12021. https://doi.org/10.1039/C2CP42448G.

(57) Ranade, P.; Takeuchi, H.; King, T.-J.; Hu, C. Work Function Engineering of Molybdenum Gate Electrodes by Nitrogen Implantation. *Electrochem. Solid-State Lett.* **2001**, *4* (11), G85. https://doi.org/10.1149/1.1402497.

(58) Ishida, Y.; Jung, J. K.; Kim, M. S.; Kwon, J.; Kim, Y. S.; Chung, D.; Song, I.; Kim, C.; Otsu, T.; Kobayashi, Y. Work Function Seen with Sub-MeV Precision through Laser Photoemission. *Commun. Phys.* **2020**, *3* (1), 158. https://doi.org/10.1038/s42005-020-00426-x.

(59) Arumugam, J.; Dhayal Raj, A.; Albert Irudayaraj, A. Solvent Effects on the Properties of Bi2S3 Nanoparticles: Photocatalytic Application. *J. Mater. Sci. Mater. Electron.* **2017**, *28* (4), 3487–3494. https://doi.org/10.1007/s10854-016-5947-6.

(60) Campanari, V.; Martelli, F.; Agresti, A.; Pescetelli, S.; Nia, N. Y.; Di Giacomo, F.; Catone, D.; O'Keeffe, P.; Turchini, S.; Yang, B.; Suo, J.; Hagfeldt, A.; Di Carlo, A. Reevaluation of Photoluminescence Intensity as an Indicator of Efficiency in Perovskite Solar Cells. *Sol. RRL* **2022**, *6* (8), 2200049. https://doi.org/10.1002/solr.202200049.

(61) Balasubramani, V.; Chandraleka, S.; Rao, T. S.; Sasikumar, R.; Kuppusamy, M. R.; Sridhar, T. M. Review—Recent Advances in Electrochemical Impedance Spectroscopy Based Toxic Gas Sensors Using Semiconducting Metal Oxides. *J. Electrochem. Soc.* **2020**, *167* (3), 037572. https://doi.org/10.1149/1945-7111/ab77a0.

(62) Bredar, A. R. C.; Chown, A. L.; Burton, A. R.; Farnum, B. H. Electrochemical Impedance Spectroscopy of Metal Oxide Electrodes for Energy Applications. *ACS Appl. Energy Mater.* **2020**, *3* (1), 66–98. https://doi.org/10.1021/acsaem.9b01965.

(63) Shen, J.; Li, Y.; Zhao, H.; Pan, K.; Li, X.; Qu, Y.; Wang, G.; Wang, D. Modulating the Photoelectrons of G-C3N4 via Coupling MgTi2O5 as Appropriate Platform for Visible-Light-Driven Photocatalytic Solar Energy Conversion. *Nano Res.* **2019**, *12* (8), 1931–1936. https://doi.org/10.1007/s12274-019-2460-2.

(64) Kim, J. H.; Ma, A.; Jung, H.; Kim, H. Y.; Choe, H. R.; Kim, Y. H.; Nam, K. M. In Situ Growth of the Bi2S3 Nanowire Array on the Bi2MoO6 Film for an Improved Photoelectrochemical Performance. *ACS Omega* **2019**, *4* (17), 17359–17365. https://doi.org/10.1021/acsomega.9b02111.

(65) Michalec, K.; Kusior, A.; Radecka, M. Photoelectrochemical Activity of the Nanostructured Electrodes Based on the SnO2/SnS2 – Heterojunction Type II vs S-Scheme Mechanism. *Appl. Surf. Sci.* **2023**, *608*, 155201. https://doi.org/10.1016/j.apsusc.2022.155201.